Journal of Applied Fluid Mechanics, Vol. 18, No. 5, pp. 1205-1216, 2025.
Available online at www.jafmonline.net, ISSN 1735-3572, EISSN 1735-3645.
https://doi.org/10.47176/jafm.18.5.3100

Parametric Study on the Backward-facing Step Height in the Mixing Chamber of Fluidic Oscillator

W. Iskandar[1], J. Julian[2], M. I. Adhynugraha[3], F. Hasim[3] and Harinaldi[4†]

[1] *Fluid Mechanics Laboratory, Department of Mechanical Engineering, Faculty of Engineering, Universitas Indonesia, Depok, Jawa Barat, 16424, Indonesia*
[2] *Department of Mechanical Engineering, Faculty of Engineering, Universitas Pembangunan Nasional Veteran Jakarta, Jakarta, 12450, Indonesia*
[3] *National Research and Innovation Agency (BRIN), Jl. M.H. Thamrin, DKI Jakarta, 10340, Indonesia*
[4] *Department of Mechanical Engineering, Faculty of Engineering, Universitas Indonesia, Depok, Jawa Barat, 16424, Indonesia*

†*Corresponding Author Email: harinald@eng.ui.ac.id*

ABSTRACT

The improvement of the fluidic oscillator as an active flow control device is studied in depth. The interior geometry of the fluidic oscillator is modified by adding backward-facing step (BFS). Variations of BFS height (H) are 2, 4, 6, 8, and 10 mm. The study is carried out computationally using OpenFoam. An unstructured mesh is used in this study, with the mesh quality maintained at y^+<5. The highest frequency increase occurs at BFS height of 10 mm, which is 36.45%. On the other hand, BFS also increases the average pressure drop by less than 5%, as observed across all height variations. Overall, this study suggests using BFS height of 10 mm. The increase in the momentum of the return flow within the feedback channel leads to a higher oscillation frequency of the fluidic oscillator. The increase in average pressure drop is due to the presence of a recirculation bubble right in the step.

Article History

Received September 17, 2024
Revised November 28, 2024
Accepted December 19, 2024
Available online March 4, 2025

Keywords:

Average pressure drop
BFS
Fluidic oscillator
Frequency
Height

1. INTRODUCTION

Flow control is a field of study that encompasses the rapidly evolving areas of fluid mechanics and fluid dynamics. Humans can produce high-quality energy conversion and conservation devices by implementing flow control. This knowledge can be used in wind turbines to work more optimally (Koklu & Owens, 2017). It will increase the system's efficiency and affect the production of electrical energy. Flow control can also significantly impact energy conservation (Kara et al., 2018). By studying flow control, the aerodynamic efficiency of vehicles will increase so that they can save fuel usage significantly (Metka & Gregory, 2015). Flow control can also be applied in the skyscraper buildings. Building collapse due to wind exposure, which causes vortex shedding, can also be avoided by studying flow control (Frank, 2018).

Flow control is very closely related to the study of boundary layers, which was first put forward by Ludwig Prandtl in 1904. In his research, Ludwig Prandtl tried to control fluid flow, especially boundary layer separation using suction and blowing methods (Anderson, 2005). In general, active flow control is a method that requires extra energy to operate, and adjustments can be made while it is operating. It differs from passive flow control, which does not require additional energy but is very difficult to adjust. Therefore, the active flow control method suits real-time and unsteady flow conditions. However, active flow control has a more significant impact than passive flow control. Many active flow control devices are available, including suction, blowing, synthetic jet, plasma actuator, fluidic oscillator, and others. The fluidic oscillator is an active flow control device that is very simple to design (Harinaldi et al., 2015).

Woszidlo et al. (2015) conducted a study on the volume rate and volume of fluid flow in a feedback channel at several bulk velocity variations. The results show that the flow rate entering the feedback channel has different values depending on the oscillation phase and bulk velocity. However, the volume of fluid entering the feedback channel is independent of bulk velocity variations. Another study compared the performance of a fluidic oscillator against a steady jet using experimental methods. The results show that the fluidic oscillator jet is superior to steady jet in terms of momentum, mass flow, and energy produced. It is caused by several things,

NOMENCLATURE

H	height of BFS	y^+	dimensionless parameter of first cell grid
i, j	indices	δ	boundary layer thickness
k	turbulent kinetic energy	ε	dissipation rate
p	order of mesh independence test	μ	dynamic viscosity of fluids
t	time	ν	kinematic viscosity of fluid
u	instantaneous velocity	ρ	density of fluid
u'	velocity fluctuation	σ	coefficients in turbulence model
$\overline{u}$	velocity average	φ	phase angle
x, y	spatial coordinates	ω	specific rate of dissipation

including a larger jet spreading angle, broader spanwise coverage, and stronger coherent vortices than the steady jet (Otto et al., 2019). Krüger et al. (2013) conducted a comparative study between computational fluid dynamics (CFD) and experimental particle image velocimetry (PIV). The results of the study show that numerical 2D modeling shows the best results, being closest to experimental results. The governing equation that produces the recommended results is Reynolds-Averaged Navier-Stokes (RANS) with the k-omega SST turbulence model. Several studies regarding fluidic oscillator can be seen in Table 1.

Tony et al. (2021) modified the concept of Integrated Microfluidic Circuits (IMCs) into Soft Microfluidic Systems (SMS). In addition, the concept of a valve mechanism for SMS was also developed. Overall, a simpler and more compatible microfluidic was produced. Farahinia et al. (2020) conducted a review study to separate circulating tumor cells (CTCs) from the blood. This has challenges, including the fact that CTCs have a shape similar to blood cells. Therefore, several solutions are offered: microfluidic technology, Lab-on-a-Chip and Lab-on-a-CD. Farahinia et al. (2023) applied microfluidic to separate CTCs from the blood. Microfluidic devices have been shown to work more efficiently and sensitively. However, further studies are still needed to improve microfluidic performance.

Portillo et al. (2021) conducted an experimental study to determine the effect of scaling down a fluidic oscillator on oscillation frequency and oscillation angle. The study was carried out experimentally using the pressure variable as input. Findings indicate that scaling down the fluidic oscillator can produce a higher oscillation frequency. However, the oscillation angle of the fluidic oscillator becomes smaller when the fluidic oscillator is scaled down. Increasing the inlet pressure can also reduce the oscillation angle in all variations of scaling down (Portillo et al., 2021). Yang et al. (2007) developed a BFS fluidic oscillator model and investigated its performance experimentally using PIV. The BFS fluidic oscillator caused an increase in the oscillation frequency and average pressure drop. The increase in the average pressure drop is higher when the mass flow rate increases.

The best of our knowledge, not much research has discussed efforts to improve the performance of fluidic oscillators. One promising way to improve the performance of fluidic oscillator is by adding BFS. However, BFS has the drawback of increasing the average pressure drop. Additionally, the use of BFS for the general model of two-feedback-channel fluidic oscillator has not yet been explored. Therefore, this is carried out to improve the performance of the fluidic oscillator from the perspective of oscillation frequency and average pressure drop by modifying BFS height (H). The height of BFS on the fluidic oscillator has also yet to be studied by previous studies and is an interesting aspect that needs further study in this research. The overall scope of this research can be seen in Table 1. This research varied the height of the BFS from 2, 4, 6, 8, and 10 mm. With this research, the development of fluidic oscillator designs will become more widespread and produce reliable fluidic oscillators.

Table 1 Several studies on fluidic oscillators

Study	RANS modelling	Characterization	Parametric Study	Common model	BFSFO	BFS modification
Woszidlo et al. (2015)	√	√	×	√	×	×
Otto et al. (2019)	×	√	×	√	×	×
Krüger et al. (2013)	√	×	×	√	×	×
Portillo et al. (2021)	×	√	×	√	×	×
Yang et al. (2007)	×	×	×	×	√	×
Seo et al. (2018)	√	√	√	√	×	×
Liu et al. (2022)	×	√	×	×	×	×
Tesař et al. (2012)	×	√	×	×	×	×
Bobusch et al. (2013)	×	√	×	√	×	×
Gaertlein et al. (2014)	×	√	×	√	×	×
Current study	√	√	√	√	√	√

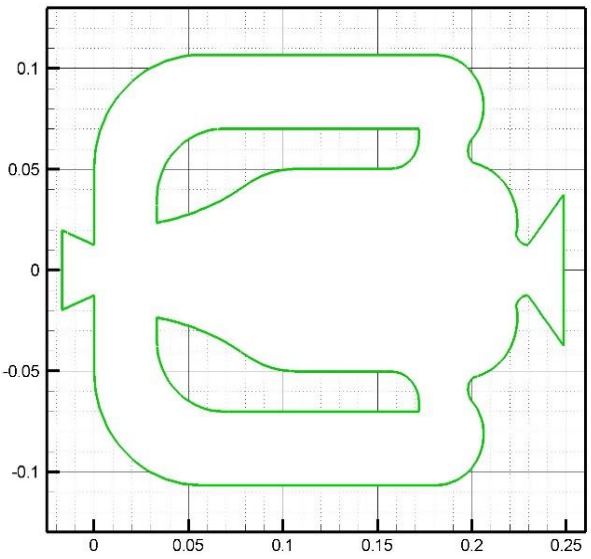

Fig. 1 Geometry of Fluidic Oscillator

2. METHODOLOGY

2.1 Fluidic Oscillator as Flow Control Devices

Implementing the fluidic oscillator as an active flow control device is an interesting choice due to its simple design. Another advantage of the fluidic oscillator is that it can operate without using moving parts and electronic components. There are several types of fluidic oscillator, but the two-feedback channel model is the most used fluidic oscillator (Tajik et al., 2021). The Coanda effect phenomenon is the mechanism by which the two-feedback-channel fluidic oscillators produce oscillating fluid flow. Initially, the fluid that enters through the inlet nozzle into the mixing chamber attach upper or lower mixing chamber (Nili-Ahmadabadi et al., 2020). Some fluid will continue moving towards the nozzle outlet, while the rest will move towards the upper or lower feedback channel (Löffler et al., 2021). The geometry of fluidic oscillator is shown in Fig. 1.

2.2 Backward-Facing Step (BFS)

The BFS is a geometric model deliberately designed to produce fluid flow separation. This fluid flow separation occurs right at the end of the step. A reattachment point follows fluid flow separation. The flow separation is filled by a primary recirculation region whose size changes and produces natural oscillations with a particular frequency. As a result, the location of the reattachment points changes on a particular time scale. Meanwhile, a secondary recirculation region can be found in the corner of the BFS. Many terms refer to BFS, including sudden expansion flows, backward flows, circular expanding flows, diverging channels, and back-step flows. Even though the BFS is a 3D geometry, the fluid flow analysis can be simplified to a 2D form while maintaining the important fluid flow features produced by the BFS (Scharnowski et al., 2017). BFS can be seen in Fig. 2 (Biswas et al., 2004).

2.3 BFS Height in Fluidic Oscillator

This research applies a BFS to the mixing chamber of the fluidic oscillator. There are two BFS installed each on the upper and lower walls of the mixing chamber. It is expected that with the presence of BFS in the mixing chamber fluidic oscillator, there will be an amplification of the oscillation fluid flow inside fluidic oscillator and the separated flow due to BFS. With this amplification, it is expected that there will be an increase in the overall oscillation frequency. Several variations of the BFS height (H) have been proposed, i.e., 2, 4, 6, 8, and 10 mm. BFS height variations are carried out to determine the ideal height to produce a BFS fluidic oscillator with high frequency and low average pressure drop. The mass flow rate for each variation is kept constant at 80 kg/h. The BFS fluidic oscillator can be seen in Fig. 3.

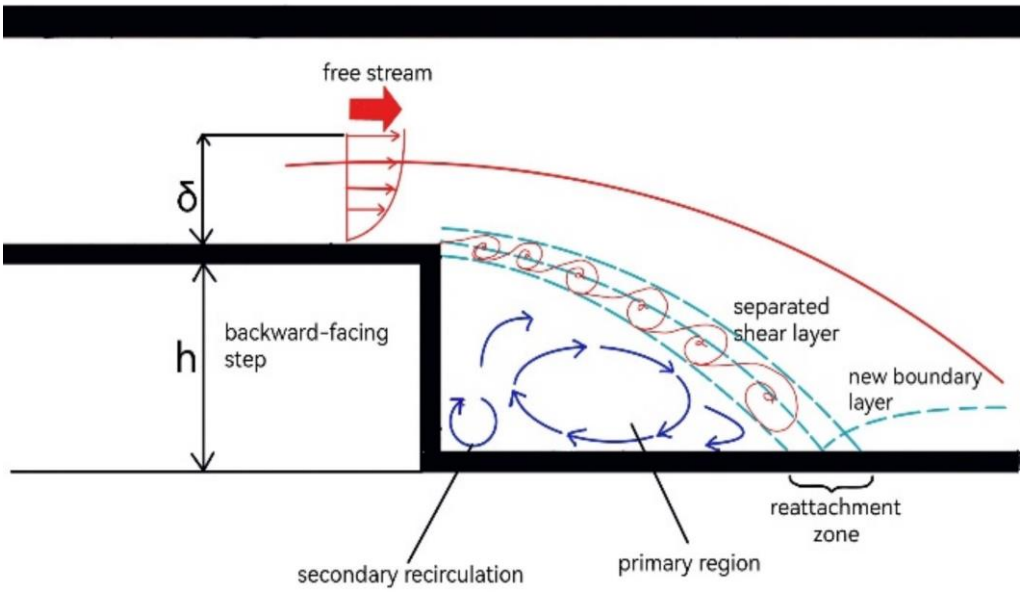

Fig. 2 BFS flow structure

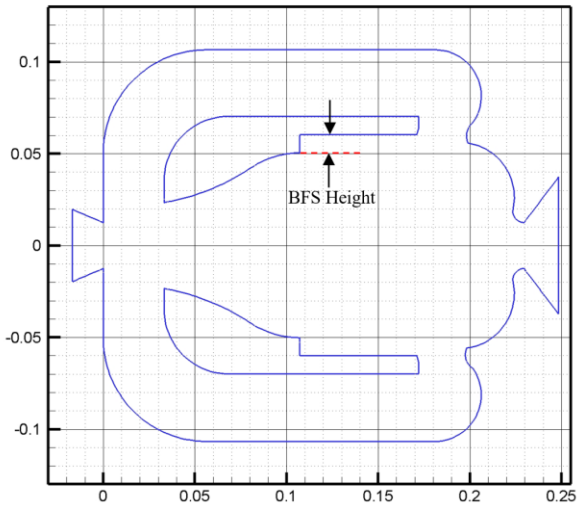

Fig. 3 BFS height to be varied

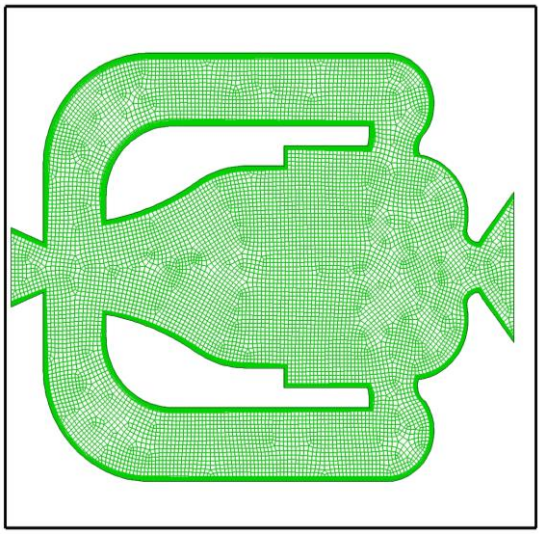

Fig. 5 Mesh on fluidic oscillator

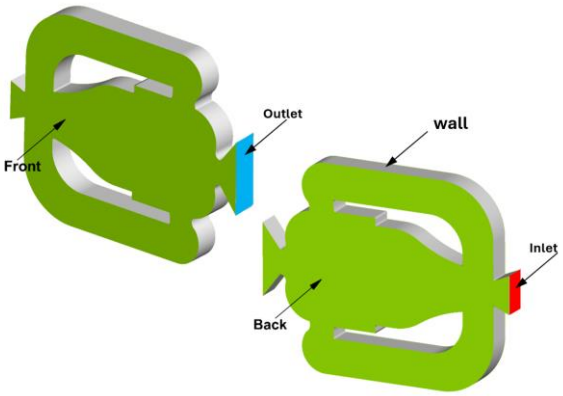

Fig. 4 Boundary condition of fluidic oscillator

2.4 Boundary Condition

The boundary condition type in the inlet of the fluidic oscillator is flowRateInletVelocity, where the fluid input is mass flow rate. At the outlet, the boundary condition is pressure-outlet, with the type of boundary condition being fixedValue. All walls in the fluidic oscillator are set as wall no-slip. Since the simulations are done with two dimensions, the boundary condition in front and back of fluidic oscillator is empty. The boundary conditions in this study can be seen in Fig. 4.

2.5 Pre-Processing

CFD involves several preparations, from the initial creation of the computer-aided design (CAD) design to the selection of governing equations. The fluidic oscillator design used is the one initially created by Bray and later published by Portillo et al. (2021). After creating a CAD design, a mesh can be formed. The mesh chosen is an unstructured mesh. Furthermore, the mesh is created in y^+<5, as in Fig. 5. After the mesh is created, the choice of governing equation can be determined. The governing equation chosen is Unsteady Reynolds-Averaged Navier-Stokes (URANS). URANS is the Navier-Stokes equation that has been modified to produce a numerical governing equation with a low iteration cost. The modification is done by averaging each variable so that the fluctuating component is equal to 0. The URANS equation is mathematically given in equations 3 and 4, which consist of the mass and momentum conservation equations, respectively (Iskandar, 2022). Meanwhile, the turbulence model to complete the RANS equation is SST k-omega. SST k-omega was chosen because it is a turbulence model that produces the best accuracy. The accuracy of SST k-omega is proven in a study by Kruger et al. (2013). In addition, this turbulence model only consists of two equations, so it has a low cost of iteration. The mathematical equation can be seen in equations 5 and 6 (Lacombe et al., 2019).

$$\frac{\partial \overline{u_i}}{\partial x_i} = 0 \tag{3}$$

$$\frac{\partial \overline{u_i}}{\partial t} + \overline{u_j}\frac{\partial \overline{u_i}}{\partial x_j} = -\frac{1}{\rho}\frac{\partial p}{\partial x_i} + \nu\frac{\partial}{\partial x_j}\left(\frac{\partial \overline{u_i}}{\partial x_j} + \frac{\partial \overline{u_j}}{\partial x_i}\right) - \frac{\partial}{\partial x_j}\left(\overline{u_i' u_j'}\right) \tag{4}$$

$$\rho\frac{Dk}{Dt} = \tau_{ij}\frac{\partial \overline{u_i}}{\partial x_j} - \beta^* k\rho\omega + \frac{\partial}{\partial x_j}\left[\left(\mu + \frac{\mu_T}{\sigma_K}\right)\frac{\partial k}{\partial x_j}\right] \tag{5}$$

$$\rho\frac{D\omega}{Dt} = \frac{\gamma}{v_t}\frac{\partial \overline{u_i}}{\partial x_j} - \beta\rho\omega^2 + \frac{\partial}{\partial x_j}\left[\left(\mu + \frac{\mu_T}{\sigma_k}\right)\frac{\partial \omega}{\partial x_j}\right] + 2\rho(1-F_1)\sigma_{\omega 2}\frac{1}{\omega}\frac{\partial k}{\partial x_j}\frac{\partial \omega}{\partial x_j} \tag{6}$$

2.6 Velocity Profile Extraction

The fluid flow in the internal fluidic oscillator is analyzed through the velocity profile. There are four straight lines created. Two lines in the mixing chamber

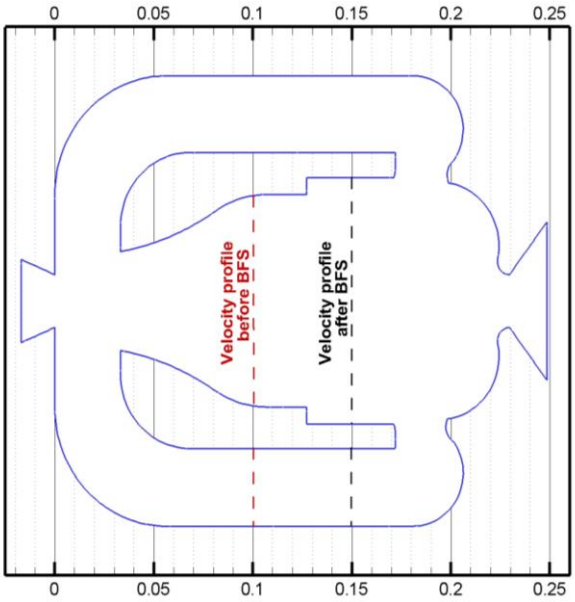

Fig. 6 Velocity profile location

consist of the before and after steps in the BFS. The remaining two are in the lower feedback channel. Velocity profile in the mixing chamber is used to observe the primary jet flow pattern in the mixing chamber. Other velocity profiles in the feedback channel are used to observe the return flow to suppress the primary jet in the mixing chamber. The specific location of the velocity profile can be seen in Fig. 6.

3. RESULTS AND DISCUSSION

The error rate of the computational results is confirmed through the validation stage. Numerical results are compared to experiments conducted by Gaertlein et al. (2014). Validation is carried out at mass flow rates ranging from 10 kg/h to 90 kg/h. The relationship between mass flow rate and oscillation frequency produced through computational results is linear. These results are similar to the experimental results. Apart from being similar in the relationship between mass flow rate and frequency, computational and experimental results also show that frequency are not much different. The results show that the highest percentage error occurs at a mass flow rate of 30 kg/h with an error of 13.94%. Meanwhile, the lowest error was observed at high mass flow rates, where at 80 kg/h and 90 kg/h, the errors produced were 1.94% and 2.09%, respectively. Overall, it can be concluded that the data from computational or numerical studies show quite satisfactory results. So that the data can be considered quite valid. Validation can be seen in Fig. 7.

Verification is a stage to check whether the mesh used for the computing process is good enough or whether improvements are needed regarding the number of elements. This process is also known as the mesh independence test which generalized by Roache (Roache, 1994). Three meshes are proposed to pass this stage: coarse with 38544 elements and element size 0.0032. Meanwhile a medium mesh has a total of 77240 elements and an element size of 0.0025. The mesh with the highest

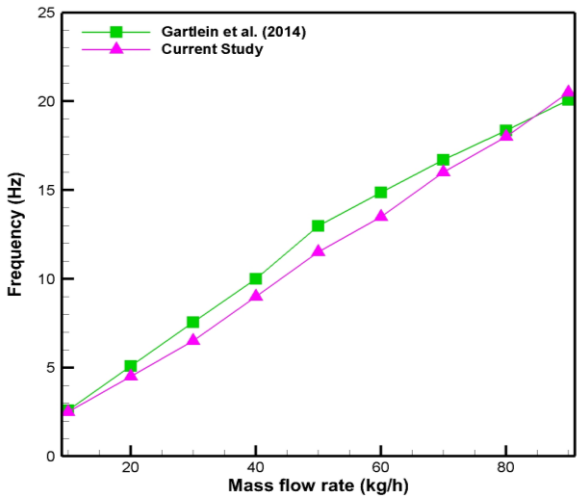

Fig. 7 Validation

Table 2 Mesh Independence Test

Mesh	*r*	Freq.	Approximation value	Error
Fine	2	23.97	23.971	0.008%
Medium		23.85		0.508%
Coarse		21.97		8.351%

number of elements is fine, with an element size of 0.002. The results of the mesh independence test can be seen in Table 2, where the number of mesh independence test results is close to 1 (Julian et al., 2023). It means that the mesh has met the convergence criteria. By calculating the error of the approximation value, it can be concluded that the mesh with fine elements shows the best results and will be used for the overall computing process.

The computational results show that using a BFS on the fluidic oscillator affects the oscillation frequency. However, the oscillation frequency varies depending on the height of the BFS. At a height of 2 mm to 6 mm, the oscillation frequency remains constant at 21.97 Hz. It means that changing the height of the BFS from 2 mm to 6 mm does not affect the oscillation frequency. When the height is changed again to 6 mm, the frequency changes quite significantly, namely 25.97 Hz. The frequency change continues if the height of the BFS is changed to 10 mm. The oscillation frequency at a height of 10 mm is 27.97 Hz. Overall, it can be concluded that if you want to produce the highest frequency, it is recommended to use a BFS height of 10 mm. A graph showing the relationship between changes in the height of the BFS and changes in the oscillation frequency produced by the fluidic oscillator can be seen in Fig. 8.

In order to obtain more comprehensive information regarding the oscillation frequency produced by the fluidic oscillator, the analysis is deepened by discussing the frequency differences compared to the baseline fluidic oscillator. This data also can be seen in Fig. 7. At heights of 2 up to 6 mm, the oscillation frequency increases when compared with the baseline. The increase is found to be 7.21%. This percentage then increases more rapidly if the height is also increased to 8 mm and 10 mm. At a height

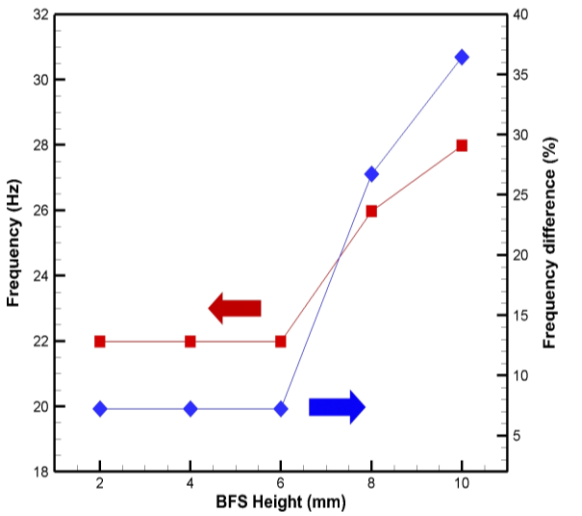

Fig. 8 Frequency of each variation

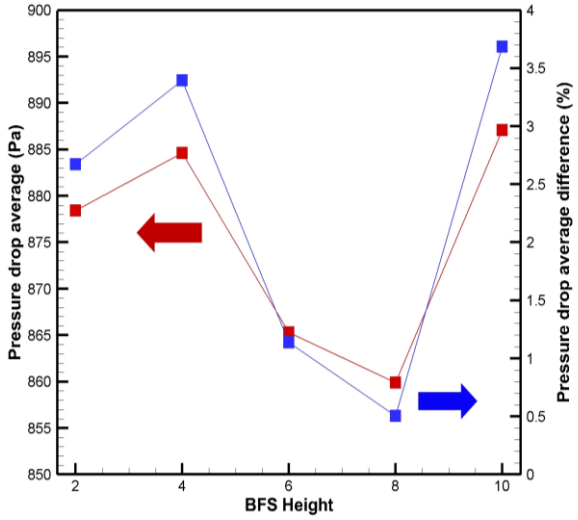

Fig. 9 Pressure drop average of each variation

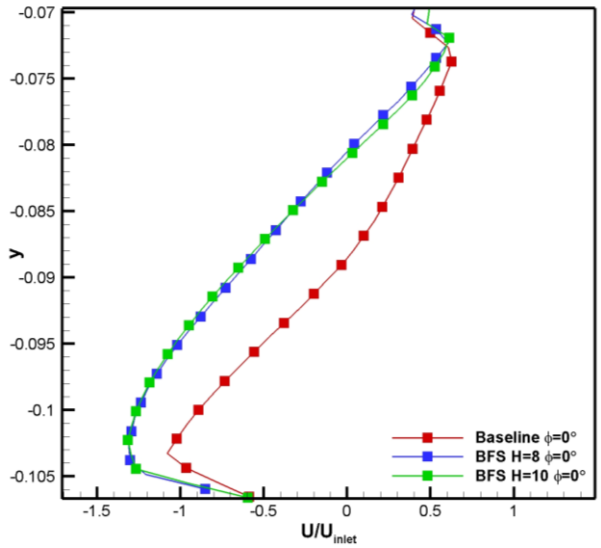

(a) phase 0°

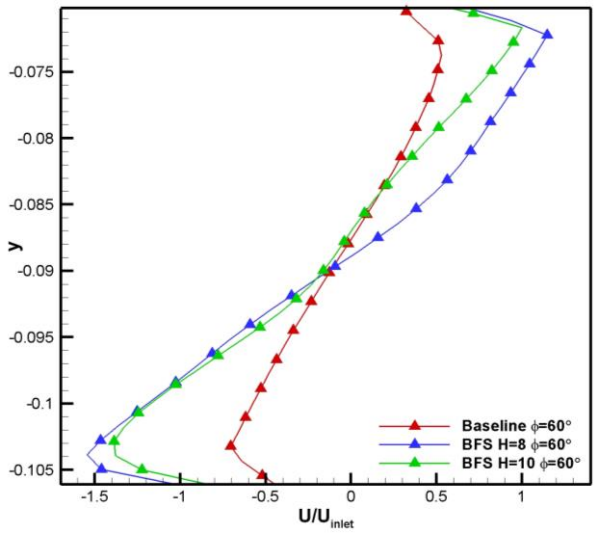

(b) phase 60°

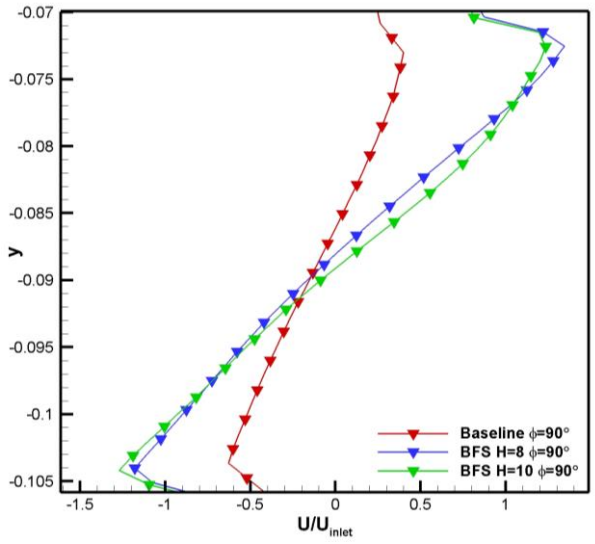

(c) phase 90°

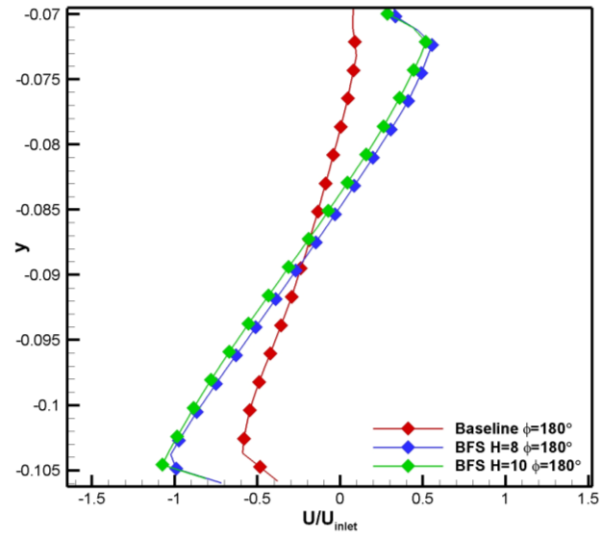

(d) phase 180°

Fig. 10 Velocity profile in the feedback channel before BFS

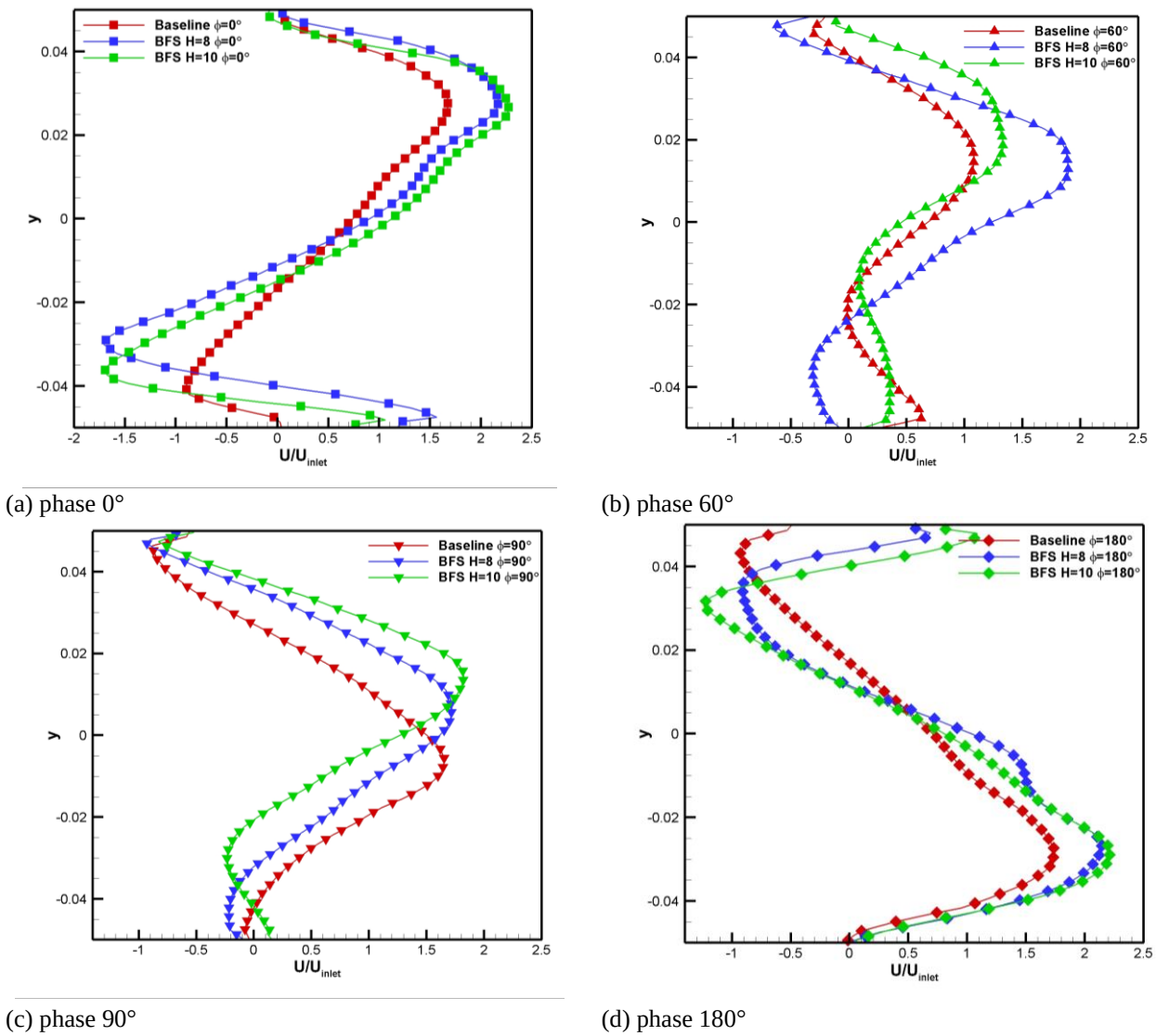

(a) phase 0° (b) phase 60°

(c) phase 90° (d) phase 180°

Fig. 11 Velocity profile in the mixing chamber before BFS

of 8 mm, there is an increase in the oscillation frequency by 26.7%. Besides that, at a height of 10 mm, there is an increase in the oscillation frequency of 36.45%. This increase in oscillation frequency is caused by BFS, which produces bubbles to encourage more fluid flow to enter the feedback channel. If the fluid flow into the feedback channel has greater mass and momentum, it can press the main jet in the mixing chamber faster to increase the oscillation process.

Average pressure drop is another parameter that must be considered in fluidic oscillator performance analysis. The average pressure drop is closely related to the energy deficit in the operation of the fluidic oscillator. The relationship between the height of the BFS and the pressure drop average is clearly shown in Fig. 9. Changes in height from 2 mm, 4 mm to 6 mm impact changes in the average pressure drop. It turns out to be in contrast when viewed from the perspective of the frequency at which the height changes from 2 mm to 6 mm less affect the frequency. The average pressure drop fluctuates with changes in the height of the BFS. It can be seen at the heights of 4 mm and 10 mm, which are experiencing an increasing trend compared to the previous height. The fluctuating average pressure drop in parametric studies was also found in Yang et al. 2024 research. Thus, it is necessary to analyze the average pressure drop difference against the baseline under the same fluid flow conditions to gain a deeper understanding.

The average pressure drop difference is a percentage difference between the average pressure drop data from each height variation and the fluidic oscillator baseline. All average pressure drops produced by the BFS fluidic oscillator are greater than the baseline fluidic oscillator, so the percentage is positive. The average pressure drop for the baseline fluidic oscillator itself is 855.56 Pa. Figure 8 shows that all height variations have a relatively small percentage increase where the increase is less than 5%. However, the lowest increase is obtained when using a BFS with a height of 8 mm, where the resulting increase was 0.506%. The highest increase occurred at the height of the BFS of 10 mm, where the increase was 3.396%.

Thus, increasing BFS height is insignificant regarding the average pressure drop. Considering the frequency and average pressure drop, it is recommended to use a fluidic oscillator with a height of 10 mm because the increase in frequency is quite high, namely 36.45%, with a relatively

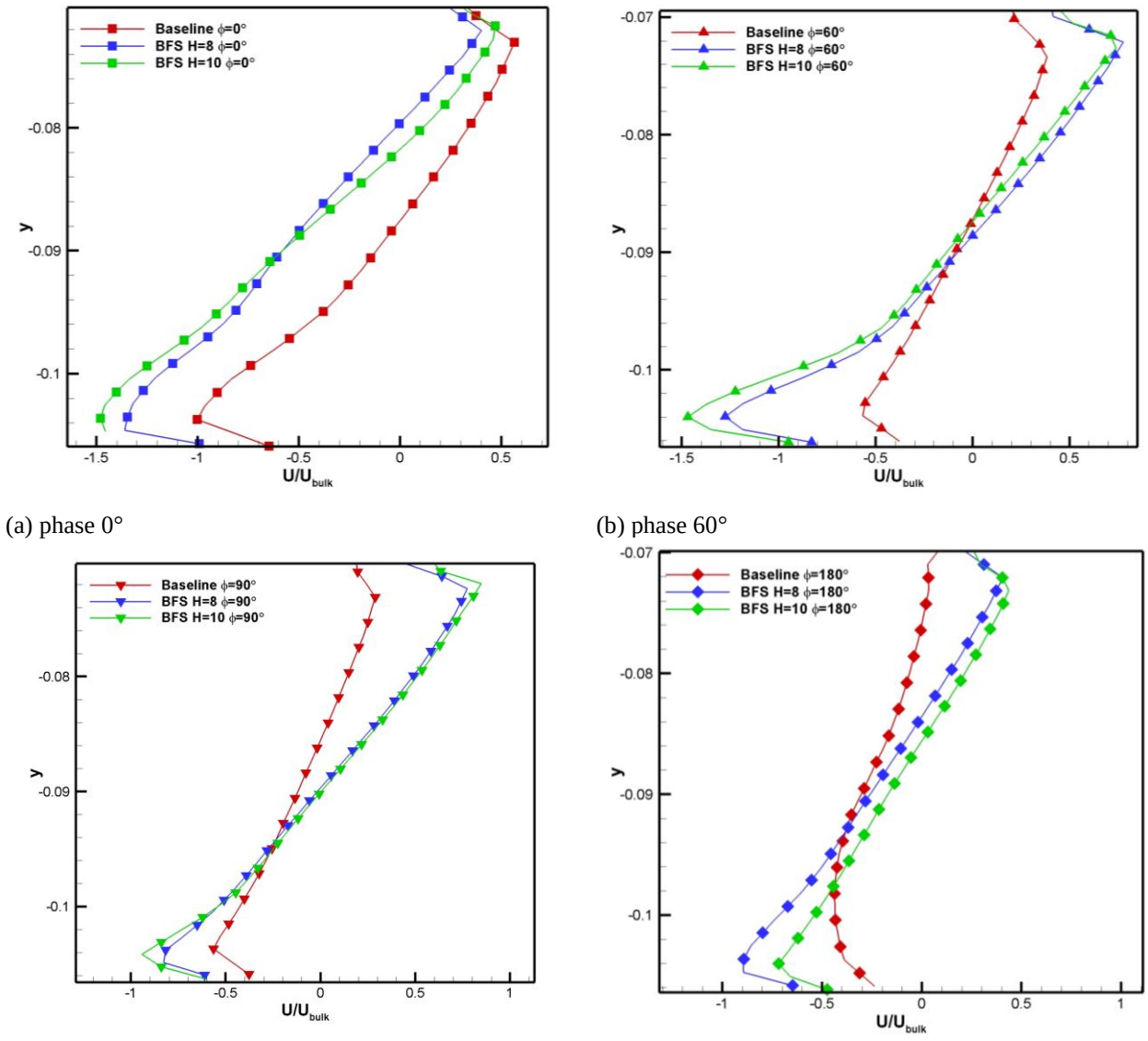

(a) phase 0° (b) phase 60°

(c) phase 90° (d) phase 180°

Fig. 12 Velocity profile in the feedback channel inline BFS

very low increase in average pressure drop, namely only 3.396%.

The BFS with a height of 8 mm and 10 mm is chosen as a sample to compare with the baseline model. The velocity profile in the lower feedback channel before going through the BFS can be seen in Fig. 10. Phase 0° occurs when the lower feedback channel is active to send a reverse flow to pressurize the main jet in the mixing chamber. The velocity profile is negative because the flow through the feedback channel is reverse flow. In other words, if look at the fluid flow in the feedback channel, the more negative the velocity value, the greater the momentum of the reverse flow. It can be seen that the use of BFS can increase the momentum in the feedback channel and suppress the main jet so that the oscillation frequency becomes greater. momentum then decreases when the phase becomes 60° because there is a shift in activity from the lower feedback channel to the upper feedback channel. Furthermore, when the oscillation phase becomes 90°, the phase crosses from lower to upper so that the velocity profile is almost symmetrical between the upper and lower half. Meanwhile, when the phase is 180°, the lower feedback channel is no longer active, and the upper feedback channel is active. So, the velocity value is relatively smaller compared to other phases.

The velocity profile in the mixing chamber before going through the BFS can be seen in Fig. 11. In phase 0°, the jet should be on the upper wall of the mixing chamber. The jet attached to the upper wall of the mixing chamber is observed in all fluidic oscillator models. This jet will then move towards the lower wall as the oscillation phase increases until it reaches the 180° phase. The difference in velocity profile is also visible in the jet in the mixing chamber. It is observed at phase 60°. The jet appears to have less momentum than BFS. In the 90° phase, the jet's transition phase, the jet is closer to the lower mixing chamber than the 60° phase. The complete 180° phase shows that the jet is attached to the lower wall of the mixing chamber.

The velocity profile in the lower feedback channel can be seen in Fig. 12. Similar to the zone before the BFS

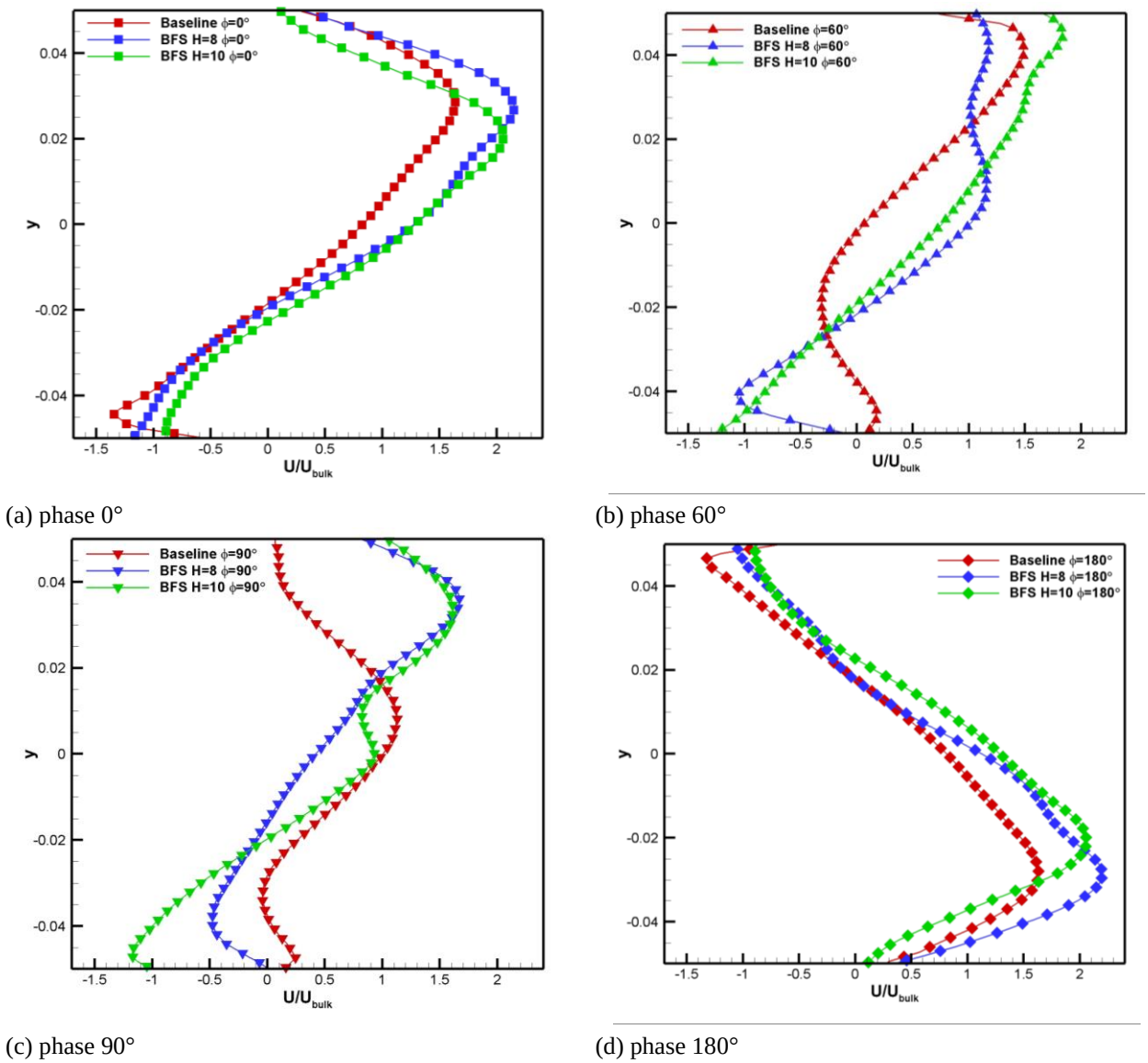

(a) phase 0° (b) phase 60°

(c) phase 90° (d) phase 180°

Fig. 13 Velocity profile in the mixing chamber inline BFS

in Fig. 10, the momentum shown by the velocity profile is greater in the fluidic oscillator with the BFS. Apart from that, height 10 mm shows a slight difference when compared to height 8 mm. Momentum at height 10 mm is greater than momentum at height 8 mm. It is done with greater frequency as well. The increase in momentum at height 10 mm is also visible at the 60° phase. If you look at the 90° phase, the characteristic velocity profile produced by the jet is the same as shown in Fig. 11(c). A slight difference occurs in the 180° phase where height 8 mm shows greater momentum than 10 mm. However, this is not significantly influenced because, at the 180° phase, the lower feedback channel is inactive in channeling the reverse flow.

Analysis of the velocity profile in the mixing chamber, especially in the BFS, can be seen in Fig. 13. In detail, the jet on the BFS shows a larger y coverage. It is a consequence of the BFS, thereby increasing the area through which fluid flows. The jet in the mixing chamber also shows that with the presence of a BFS, there is a significant increase in momentum. However, this difference is insignificant when compared between height 8 mm and height 10 mm. This discussion is very relevant in phases 0° and 180°. In the 60° phase, there is a change in the fluid flow pattern for BFS FO where the velocity profile produces more than one maximum peak. It is due to the jet being split and spread out. The characteristics of this jet will be very easy to see on the velocity contour. In phase 90°, the characteristics of the jet produced are the same as those of the jet in the mixing chamber before passing through the mixing chamber. Phase 180° also shows that the jet is perfectly attached to the lower wall mixing chamber.

The fluid flow streamlines in the fluidic oscillator for the baseline and BFS models is depicted in Fig. 14. When the oscillation phase of the fluidic oscillator is 0°, the recirculation bubble is right in the lower wall mixing chamber, and the primary jet is in the upper wall mixing chamber. It is observed in the baseline fluidic oscillator and BFS. Apart from that, several small bubbles around the main bubble are much larger. The center of the small bubble is not exactly near the step, so the increase in average pressure drop is not very significant compared to the baseline model (Yang et al., 2007). This large bubble

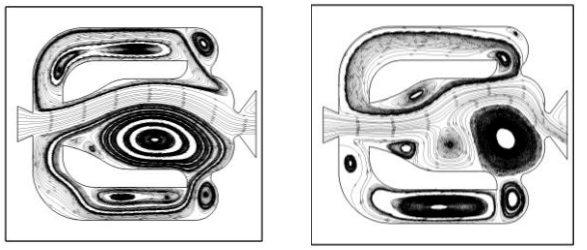

(a) baseline phase 0° (b) baseline phase 60°

(c) baseline phase 90° (d) baseline phase 180°

(e) BFS H=8 phase 0° (f) BFS H=8 phase 60°

(g) BFS H=8 phase 90° (h) BFS H=8 phase 180°

(i) BFS H=10 phase 0° (j) BFS H=10 phase 60°

(k) BFS H=10 phase 90° (l) BFS H=10 phase 180°

Fig. 14 Streamline

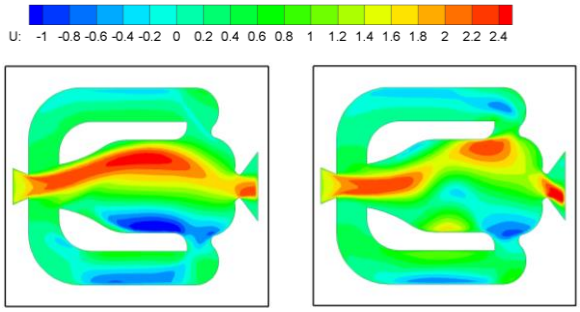

(a) baseline phase 0° (b) baseline phase 60°

(c) baseline phase 90° (d) baseline phase 180°

(e) BFS H=8 phase 0° (f) BFS H=8 phase 60°

(g) BFS H=8 phase 90° (h) BFS H=8 phase 180°

(i) BFS H=10 phase 0° (j) BFS H=10 phase 60°

(k) BFS H=10 phase 90° (l) BFS H=10 phase 180°

Fig. 15 normalized x-component Velocity contour

then becomes smaller as the phase develops and appears on the upper wall of the mixing chamber. The appearance of bubbles on the upper wall is first observed in the baseline model, where at the 60° phase, the bubbles for the baseline were much larger compared to the BFS model. The bubble for the BFS model appears to enlarge at the 90° phase and then reaches a perfect shape at the 180° phase. On the other hand, the bubble that previously formed in the lower wall of the mixing chamber slowly becomes smaller as the phase increases until it completely disappears at phase180°.

The global velocity distribution can be seen in the velocity contour. At phase 0°, it can be seen that the jet is attaching to the upper wall and is then followed by the lower wall mixing chamber which is becoming a return flow channel (Portillo et al., 2022). A fairly large negative velocity characterizes this. The transition phase at the 60° phase also shows conditions in the lower feedback channel where the momentum decreases while the momentum in the upper feedback channel continues to increase. The main jet in the mixing chamber has also been separated from the mixing chamber. At phase 90°, it tends towards the center, moves to the lower mixing chamber, and is followed by the upper feedback channel, which is increasingly filled with reverse flow. It is caused by a more intensive mixing process in the mixing chamber due to flow separation with varying sizes according to certain natural frequencies, thereby pressuring the fluid to move more toward the feedback channel. Phase 180° has shown the jet attached to the lower wall mixing chamber. The velocity contour for the fluidic oscillator can be seen in Fig. 15.

4. CONCLUSION

Modifications are made to the geometric structure of the two-feedback channel fluidic oscillator by applying a BFS at the location of the mixing chamber of the fluidic oscillator. The height varies to obtain a best-performing model. The height of BFS in the mixing chamber varied at 2, 4, 6, 8 and 10 mm. The performance of the fluidic oscillator is seen from the frequency and pressure drop average. BFS increased the oscillation frequency produced by the fluidic oscillator. At heights of 2, 4, and 6 mm, it is known that the increase in frequency is 7.21%. This increase in frequency continues to increase to 26.7% when the height of the BFS becomes 8 mm. If the height is increased again to 10 mm, then the percentage increase in frequency is 36.45%. The average pressure-drop shows that there is an increase when the BFS is applied. However, this increase is not significant, where the average pressure drops increases less than 5%. Thus, a BFS with a height of 10 mm is recommended. The increase in frequency in the BFS fluidic oscillator is caused by an increase in momentum in the feedback channel so that it can suppress the primary jet in the mixing chamber to move towards another wall of the mixing chamber immediately. The increase in average pressure drop is caused by secondary recirculation bubbles appearing right at the step.

Through this study, there is an increase in the performance of the fluidic oscillator, especially from the perspective of oscillation frequency. The increased oscillation frequency is expected to make fluidic oscillators more suitable for aerodynamic applications, as it will not require jet input with a high mass flow rate. In other words, there is a decrease in the minimum input value so that energy savings occur. Through these energy savings, the aircraft is expected to operate more fuel efficiently. If fuel savings occur, emissions resulting from combustion can also be reduced. This certainly has a positive impact on the environment.

ACKNOWLEDGEMENTS

The authors would like to thank the Ministry of Education, Culture, Research and Technology (Kementrian Pendidikan, Kebudayaan, Riset, dan Teknologi) through grants Pendidikan Magister menuju Doktor untuk Sarjana Unggul (PMDSU) scheme for supporting this research with grant number NKB-937/UN2.RST/HKP.05.00/2024. This grant greatly contributed to the success of the research and publication of this article.

CONFLICT OF INTEREST

The authors declare that they have no known competing financial interests or personal relationships that could have influenced or appeared to influence the work reported in this paper.

AUTHORS CONTRIBUTION

W. Iskandar: Conceptualization and Writing – original draft. **J. Julian:** Review and Supervision. **M. I. Adhynugraha:** Methodology and Review. **F. Hasim:** Review and Supervision. **Harinaldi:** Supervision and Funding Acquisition.

REFERENCES

Anderson, J. D. (2005). Ludwig prandtl's boundary layer. *Physics Today*, *58*(12), 42–48. https://doi.org/10.1063/1.2169443

Biswas, G., Breuer, M., & Durst, F. (2004). Backward-facing step flows for various expansion ratios at low and moderate reynolds numbers. *Journal of Fluids Engineering, Transactions of the ASME*, *126*(3), 362–374. https://doi.org/10.1115/1.1760532

Bobusch, B. C., Woszidlo, R., Bergada, J. M., Nayeri, C. N., & Paschereit, C. O. (2013). Experimental study of the internal flow structures inside a fluidic oscillator. *Experiments in Fluids*, *54*(6), 1559. https://doi.org/10.1007/s00348-013-1559-6

Farahinia, A., Zhang, W. J., & Badea, I. (2020). Circulating tumor cell separation of blood cells and sorting in novel microfluidic approaches: a review. *Preprints*. https://doi.org/10.20944/preprints202010.0622.v1

Farahinia, A., Zhang, W., & Badea, I. (2023). Recent developments in inertial and centrifugal microfluidic

systems along with the involved forces for cancer cell separation: a review. *Sensors*, *23*(11), 5300. https://doi.org/10.3390/s23115300

Frank, W. (2018). *Building aerodynamics*. Handbook of flow visualization (pp. 661–666). Routledge.

Gaertlein, S., Woszidlo, R., Ostermann, F., Nayeri, C., & Paschereit, C. O. (2014). The time-resolved internal and external flow field properties of a fluidic oscillator. *52nd Aerospace Sciences Meeting*, 1143. https://doi.org/10.2514/6.2014-1143

Harinaldi, H., Budiarso, B., Julian, J., & WS, A. (2015). *Drag reduction in flow separation using plasma actuator in a cylinder model*. https://repo-dosen.ulm.ac.id//handle/123456789/8588

Iskandar, W. (2022). Study of airfoil characteristics on NACA 4415 with reynolds number variations. *International Review on Modelling and Simulations (IREMOS)*, *15*(3), 162–171. https://doi.org/10.15866/iremos.v15i3.21684

Julian, J., Iskandar, W., & Wahyuni, F. (2023). Effect of mesh shape and turbulence model on aerodynamic performance at NACA 4415. *Journal of Applied Fluid Mechanics*, *16*(12), 2504–2517. https://doi.org/10.47176/jafm.16.12.1983

Kara, K., Kim, D., & Morris, P. J. (2018). Flow-separation control using sweeping jet actuator. *AIAA Journal*, *56*(11), 4604–4613. https://doi.org/10.2514/1.J056715

Koklu, M., & Owens, L. R. (2017). Comparison of sweeping jet actuators with different flow-control techniques for flow-separation control. *AIAA Journal*, *55*(3), 848–860. https://doi.org/10.2514/1.J055286

Krüger, O., Bobusch, B. C., Woszidlo, R., & Paschereit, C. O. (2013). *Numerical modeling and validation of the flow in a fluidic oscillator*. 21st AIAA Computational Fluid Dynamics Conference. https://doi.org/10.2514/6.2013-3087

Lacombe, F., Pelletier, D., & Garon, A. (2019). Compatible wall functions and adaptive remeshing for the k-omega SST model. *AIAA Scitech 2019 Forum*, 2329. https://doi.org/10.2514/6.2019-2329

Liu, G., Bie, H., Hao, Z., Wang, Y., Ren, W., & Hua, Z. (2022). Characteristics of cavitation onset and development in a self-excited fluidic oscillator. *Ultrasonics Sonochemistry*, *86*, 106018. https://doi.org/https://doi.org/10.1016/j.ultsonch.2022.106018

Löffler, S., Ebert, C., & Weiss, J. (2021). Fluidic-oscillator-based pulsed jet actuators for flow separation control. *Fluids*, *6*(4). https://doi.org/10.3390/FLUIDS6040166

Metka, M., & Gregory, J. W. (2015). Drag reduction on the 25-deg Ahmed model using fluidic oscillators. *Journal of Fluids Engineering, Transactions of the ASME*, *137*(5). https://doi.org/10.1115/1.4029535

Nili-Ahmadabadi, M., Cho, D. S., & Kim, K. C. (2020). Design of a novel vortex-based feedback fluidic oscillator with numerical evaluation. *Engineering Applications of Computational Fluid Mechanics*, *14*(1), 1302–1324. https://doi.org/10.1080/19942060.2020.1826360

Otto, C., Tewes, P., Little, J. C., & Woszidlo, R. (2019). Comparison between fluidic oscillators and steady jets for separation control. *AIAA Journal*, *57*(12), 5220–5229. https://doi.org/10.2514/1.J058081

Portillo, D. J., Hoffman, E. N. A., Garcia, M., Lalonde, E. J., & Hernandez, E. (2021). *Modal analysis of a sweeping jet emitted by a fluidic oscillator.* AIAA Aviation and Aeronautics Forum and Exposition, AIAA AVIATION Forum 2021. https://doi.org/10.2514/6.2021-2835

Portillo, D. J., Hoffman, E., Garcia, M., LaLonde, E., Combs, C., & Hood, R. L. (2022). The effects of compressibility on the performance and modal structures of a sweeping jet emitted from various scales of a fluidic oscillator. *Fluids*, *7*(7), 251. https://doi.org/10.3390/fluids7070251

Roache, P. J. (1994). Perspective: A method for uniform reporting of grid refinement studies. *Journal of Fluids Engineering*, *116*(3), 405–413. https://doi.org/10.1115/1.2910291

Scharnowski, S., Bolgar, I., & Kähler, C. J. (2017). Characterization of turbulent structures in a transonic backward-facing step flow. *Flow, Turbulence and Combustion*, *98*(4), 947–967. https://doi.org/10.1007/s10494-016-9792-8

Seo, J. H., Zhu, C., & Mittal, R. (2018). Flow physics and frequency scaling of sweeping jet fluidic oscillators. *AIAA Journal*, *56*(6), 2208–2219. https://doi.org/10.2514/1.J056563

Tajik, A. R., Kara, K., & Parezanović, V. (2021). Sensitivity of a fluidic oscillator to modifications of feedback channel and mixing chamber geometry. *Experiments in Fluids*, *62*(12), 250. https://doi.org/10.1007/s00348-021-03342-0

Tesař, V., Zhong, S., & Rasheed, F. (2012). New fluidic-oscillator concept for flow-separation control. *AIAA Journal*, *51*(2), 397–405. https://doi.org/10.2514/1.J051791

Tony, A., Rasouli, A., Farahinia, A., Wells, G., Zhang, H., Achenbach, S., Yang, S. M., Sun, W., & Zhang, W. (2021). *Toward a soft microfluidic system: concept and preliminary developments.* 2021 27th International Conference on Mechatronics and Machine Vision in Practice (M2VIP), 755–759. https://doi.org/10.1109/M2VIP49856.2021.9665022

Woszidlo, R., Ostermann, F., Nayeri, C. N., & Paschereit, C. O. (2015). The time-resolved natural flow field of a fluidic oscillator. *Experiments in Fluids*, *56*(6), 125. https://doi.org/10.1007/s00348-015-1993-8

Yang, J. T., Chen, C. K., Tsai, K. J., Lin, W. Z., & Sheen, H. J. (2007). A novel fluidic oscillator incorporating step-shaped attachment walls. *Sensors and Actuators A: Physical*, *135*(2), 476–483. https://doi.org/10.1016/j.sna.2006.09.016